www.sciencemag.org/cgi/content/full/science.1209524/DC1

Supporting Online Material for

Single-Shot Correlations and Two-Qubit Gate of Solid-State Spins

K. C. Nowack,* M. Shafiei, M. Laforest, G. E. D. K. Prawiroatmodjo, L. R. Schreiber, C. Reichl, W. Wegscheider, L. M. K. Vandersypen*

*To whom correspondence should be addressed. E-mail: k.c.nowack@tudelft.nl, l.m.k.vandersypen@tudelft.nl

Published 4 August 2011 on *Science* Express
DOI: 10.1126/science.1209524

This PDF file includes:

Contents

A Materials and methods

The GaAs/(Al,Ga)As heterostructure from which the sample was fabricated was grown in the group of W. Wegscheider. The 2DEG has a mobility of $3.6 \times 10^5 \mathrm{cm}^2/\mathrm{Vs}$ and an electron density of $1.2 \times 10^{11} \mathrm{cm}^{-2}$ determined at 4.2 K. The measurements were

performed in an Oxford Instruments Kelvinox 400 HA dilution refrigerator operating at a base temperature of 80-100 mK. For real time data acquisition we use a digital oscilloscope (LeCroy Waverunner 44Xi) typically running at 250 kS/s or 500 kS/s. One of the two current/voltage converters used to record the QPC responses is identical to the one described in Ref. (*34*) and the other is an almost identical copy. Also the dc wiring and filtering is very similar to Ref. (*34*). For the gate settings of the presented measurements, the right QPC is more sensitive to changes in the charge state of the double quantum dot than the left QPC, because it exhibits a resonance, which can be tuned using the three most right gates on the sample. The left and right QPC are biased with opposite polarity, therefore we subtract the two QPC signals when analyzing real time data. In this way interference which results from e.g. mechanical noise in the cryostat or interference from the power grid (mostly) cancels out while the signal adds up (tunnel events are also visible in the most distant QPC). One dominant source of mechanical noise observed at frequencies of 6-8 kHz is the flow of helium into the 1K pot, we therefore close the needle valve of the 1K pot while acquiring real time data.

The gates LP and RP are fitted with homemade resistive bias tees ($R = 10$ MΩ, $C = 47$ nF) to allow fast pulsing of the dot levels while also maintaining a DC bias on LP and RP. The pulses are generated by an arbitrary waveform generator (Tektronix AWG 5014), which we run in the normal output mode at an amplitude setting of 4.0V$_{p-p}$, since most measurements require pulse amplitudes of several tens of mV at the sample (in both lines we have 9dB attenuation at room temperature and 30dB attenuation inside the cryostat). Per data point presented in Fig.1-4 we typically acquire 3000-5000 AWG cycles. The corresponding pulse sequence is continuously sent from the arbitrary waveform generator. A disadvantage of using bias tees is that the DC component of a pulse sequence is blocked. When changing the amplitude or duration of one stage in the pulse sequence, the DC component changes, which effectively offsets

the dot levels during the new pulse sequence compared to the previous. To avoid this effect we choose to add an additional stage to the end of the complete pulse sequence with a typical length of 3-4 ms and an amplitude such that the DC component of the pulse sequence is zero.

B Detection of electron tunneling events

B.1 Detection method

In this section we describe the method which we use to detect an event in the real time data. In principle a simple threshold detection is possible, however, the method described here allows us to improve the detection of short steps. This method has the important advantage that it is only sensitive to *changes* in current during each analyzed cycle and is therefore insensitive to slow drifts in the absolute current value. The two segments corresponding to the read-out of the left and right dot are analyzed in the same way.

Let I denote the vector with N elements containing the QPC signal during the read-out of one of the two quantum dots (N is determined by the length of the read-out stage times the sampling rate of the digital oscilloscope used for data acquisition). We define a threshold κ which we vary from the maximum value to the minimum value of I in N_κ steps. For each threshold κ we perform a threshold detection on I which results in a digital vector with N elements $I^D_\kappa(i) = -1$ if $I(i) < \kappa$ and $I^D_\kappa(i) = 1$ if $I(i) \geq \kappa$ with $i = 1, ..., N$. From the digital vector for each threshold κ we compute the following quantity: $\chi_\kappa = \frac{1}{N}\sum_{i=1}^{N} I(i) \cdot I^D_\kappa(i)$. For each analyzed shot we record the maximum value $\chi_{max} = \max(\chi_\kappa)$. Whether or not we declare that a tunnel event occurred is decided by comparing the value χ_{max} to a threshold which we denote by λ. We will

discuss how to choose λ in the next section. In addition to χ_{max} we also record the value of κ at which the digital trace I_κ^D is fluctuating the most between 1 and -1. Unless a trace contains a long tunnel event, this value can be used as an offset per cycle, since the digital trace displays most fluctuations, when κ is lying in the noise of the baseline. We use this offset to correct for slow drift of the total current value. If there is a long tunnel event, the offset determined in this way is shifted by roughly the signal height. In this case, we use the offset of the previous cycle. The correction for slow drift is used in the conditional analysis discussed in section B.3.

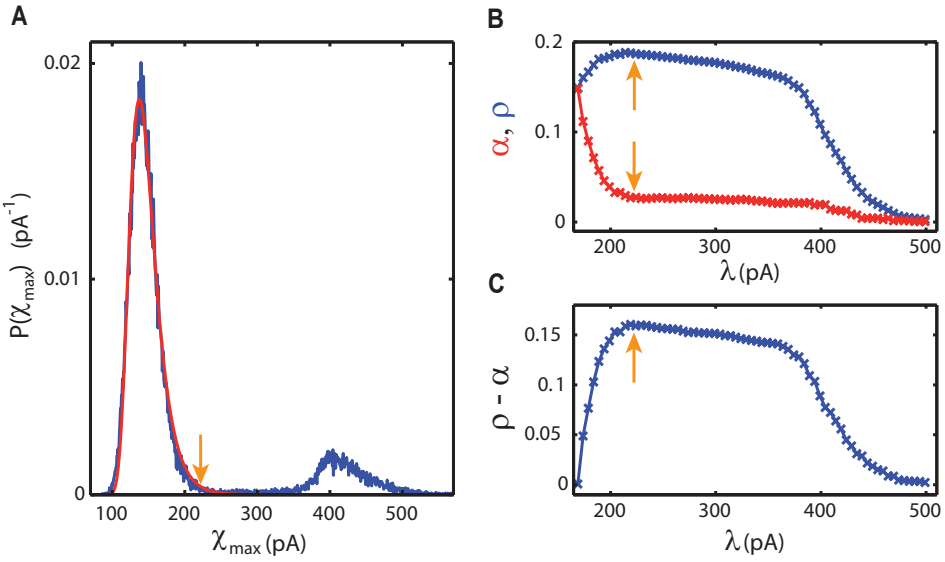

Figure S1: (A) Distribution of χ_{max}. The red line is a fit to the function given in eq. S1. The orange arrow indicates where the fitted distribution has decayed to 2% of its full height and therefore marks the chosen value for the threshold λ. (B) Amplitude ρ and offset α of exponential fits to the spin relaxation of the right dot (see Fig. S3A) as a function of the threshold λ. The orange arrows marks the value of λ which is obtained from (A). (C) The difference of ρ and α versus the threshold λ. This difference reflects the measurement contrast between spin-up and spin-down. We see that the choice of λ made in (A) also maximizes the measurement contrast.

B.2 Choosing the threshold

Here we discuss how we choose the threshold λ. In Fig. S1A we show a distribution

of the value χ_{max} obtained from a histogram of all segments of the right dot in the measurement shown in Fig. 1D. The histogram displays two peaks. One dominant peak at lower values of χ_{max} corresponding to segments which do not contain an event and a smaller peak at higher values of χ_{max} corresponding to segments which do contain an event. We fit the dominant peak with the following asymmetric distribution:

$$P(\chi_{max}) = A \cdot e^{-\Gamma(\chi_{max}-\chi^0_{max})-e^{-\Gamma(\chi_{max}-\chi^0_{max})}} \tag{S1}$$

where A is the amplitude, Γ the width and χ^0_{max} the position of the maximum.
This distribution is the asymptotic distribution of the maximum of a Gaussian process (*35*). The value of χ_{max} for segments without an event is not directly the maximum of the signal during the read-out stage, but it is strongly related to it. The distribution $P(\chi_{max})$ qualitatively captures the experimental distribution of χ_{max}. The threshold λ is chosen as the value at which the fitted distribution has decayed to 2% of its full height on the upper side of the maximum. This choice is based on the following analysis:
By analyzing measurements of the relaxation of a spin using different thresholds λ we can investigate the influence of λ on the read-out fidelities. For each threshold λ we fit the decay of the spin down probability with an exponential $P_\downarrow = \rho \cdot e^{-\Gamma_1 \cdot t} + \alpha$ where ρ is the amplitude, $\Gamma_1 = 1/T_1$ the spin relaxation rate and α the saturation value. Fig. S1B and S1C shows ρ, α and $\rho - \alpha$ as a function of the threshold λ. The value of λ at which the fitted distribution (see Fig. S1A) is at 2% of its maximum value is marked with an orange arrow. Around this value of λ, ρ and α vary only very little and $\rho - \alpha$ which is a measure for the fidelity of reading spin down (more precisely ρ is the product of spin-down fidelity and the probability to inject a spin down) is maximum at or close to this value. We repeated this analysis for several relaxation measurements and the λ obtained by our criterion results in an optimum or close to optimum threshold. We therefore use this criterion to analyze all the data presented in this report.

B.3 Conditional analysis

We perform a postselection on the data to avoid the following errors. First, when measuring the spin relaxation as e.g. shown in Fig. 1D, injection of electrons into the double quantum dot and the waiting interval during which we allow spins to relax take place in the same stage of the complete measurement cycle. For short wait times it is possible that the electrons are not yet both loaded into the double dot at the end of this stage. Second, if during the read-out of the first dot an electron tunnels out of the dot, it is possible that the dot remains empty until the end of the first read-out stage. This results in measurement cross-talk, which favors the reading of $\downarrow\downarrow$ as explained in the following. For convenience let us assume we read the right dot first. If an electron leaves the right dot during the first read-out stage, we will detect spin-down for the right dot. If the right dot is not occupied again at the end of the read-out stage, we begin the read-out of the left dot, while being in the $(1,0)$ charge state. At the read-out position of the left dot the left electron can tunnel to the right dot, followed by an electron tunneling into the left dot: $(1,0) \rightarrow (0,1) \rightarrow (1,1)$. We therefore detect a tunnel event in the left dot and consequently also declare spin-down in the left dot. In total this results in a $\downarrow\downarrow$ reading, regardless of the spin state of the left electron.

Both errors can be avoided by determining in all cycles the charge occupation of the double quantum dot at the end of the respective stages by the value of the QPC current. During the analysis we therefore record the average current corrected by an offset for each cycle (the offset is determined as discussed in section B.1) during the last 20 μs of the corresponding stage, which we denote by $\overline{I}$. The distribution of $\overline{I}$ (obtained from a histogram) shows a dominant peak corresponding to those cycles in which the double quantum dot is in the (1,1) charge state at the end of the stage and a second very broad and shallow peak corresponding to those cycles in which the double quantum dot is only

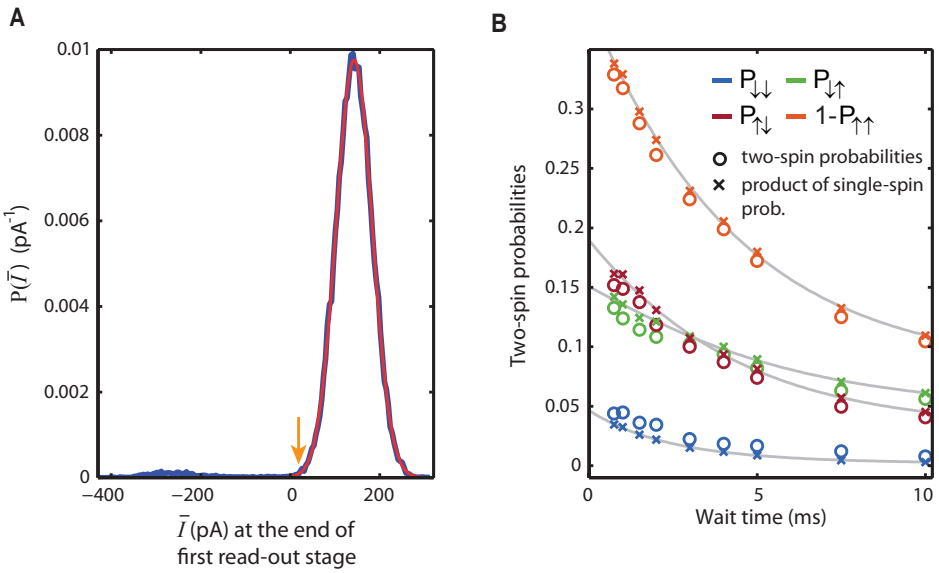

Figure S2: (A) Distribution of the average current $\overline{I}$ during the last 20 μs of the first read-out stage. The orange arrow marks the position where the distribution has decayed to 1% of its full height. All cycles for which $\overline{I}$ is smaller than this value will be discarded in the analysis. (B) Same data as in Fig. 1E but without discarding cycles in which the double dot is in a $(1, 0)$ charge state at the end of the first read-out stage. The two-spin probabilities and the product of the single-spin probabilities do not overlap, because the error coming from the now included cycles favors a $\downarrow\downarrow$ reading which introduces (artificially) correlations between measurement outcomes.

occupied with one electron at the end of the stage, see Fig. S2A. We fit the dominant peak with a Gaussian distribution and exclude all cycles from the analysis which have a value $\overline{I}$ smaller than the value at which the distribution has decayed to 1% of its full height (see Fig. S2A). This value is chosen such that we exclude the mentioned errors with a high probability, but still do not exclude an unnecessarily high number of cycles. In Fig. S2B we show the data of Fig. 1D without correcting for the above explained source of measurement cross-talk.

C Characterization of the fidelities

In this part we discuss how we can obtain the read-out fidelities from our data. In the way as is described here we find the four read-out fidelities for the measurement shown in Fig. 2B to be 95% and 95% for spin-up states in the right and left dot, and 74.7% and 71.5% for spin-down states in the right and left dot, respectively. These values are used to calculate the saturation value of the grey lines in Fig. 2B. For the measurements presented in Fig. 4 we find 95.7% and 95.0% for spin-up states in the right and left dot, and 77.7% and 78.0% for spin-down states in the right and left dot, respectively. The fidelities are different for the two measurements, because the double dot was tuned into slightly different regimes, affecting the tunnel rates and the spin relaxation times, which influence the read-out fidelities as described in the following sections.

C.1 Analytic expressions for the fidelities

Considering that we read out the spin state of each quantum dot independently, we can write the two spin state read-out fidelities as the product of the single spin read-out fidelities, $\mathcal{F}_{ij} = \mathcal{F}_i^L \cdot \mathcal{F}_j^R$ where $i, j \in \{\uparrow, \downarrow\}$ and L (R) denotes the left (right) quantum dot. This assumption is valid as long as there is no cross-talk between the read-out of the left and right spin, which is a good approximation in the case of our measurements, as discussed in the main text. The single dot fidelities are calculated differently from those in Ref. (*14*), because we have two separate and consecutive read-out stages of finite duration.

We start with the fidelity for the spin-up state, $\mathcal{F}_\uparrow = 1-\alpha$, where α is the probability that a step is detected in the QPC current although there was a spin-up state in the quantum dot. This can occur if the QPC current exceeds the threshold even though the electron stayed in the dot (refered to as a signal processing error), or if the electron

tunnels out of the dot due to thermal or electric field fluctuations. We can determine α directly for each quantum dot by initializing it in the spin-up state and successively reading it out. In this case, the fraction of the cases where a spin-up electron is declared spin-down directly gives α, see Figure S3A. α may be slightly different for the first and second read-out stage due to differences in the respective tunnel barriers, in the length of the read-out stages, in the thresholds and in the signal heights.

Next, we estimate the fidelity for the spin-down state based on the relaxation time (T_1, which can also be extracted from Fig. S3A), the duration of the read-out stage (T_R), the electron tunneling rates (denoted by Γ^i_σ where $i \in \{\uparrow, \downarrow\}$ is the spin state and $\sigma \in \{in, out\}$ represents tunneling in or out of the quantum dot) and an analysis of the measurement bandwidth. For these quantities, we leave out the labels referring to the dot that is read-out first/second for brevity.

The spin-down fidelity for the first read-out stage is $\mathcal{F}^{1st}_\downarrow = \Xi^{1st} + \Lambda^{1st}$, where Ξ and Λ are defined as follows:

The probability that a spin-down electron tunnels out during the read-out stage before it relaxes and then tunnels back into the dot is given by

$$\xi = \int_0^{T_R} \Gamma^\downarrow_{out} P_\downarrow(t) \int_0^{T_R - t} \Gamma^\uparrow_{in} e^{-\Gamma^\uparrow_{in}\tau} d\tau dt \tag{S2}$$

where $\Gamma^\downarrow_{out} P_\downarrow(t)$ is the probability density function for a spin-down electron to tunnel out at time t. The probability for the electron to be spin-down $P_\downarrow(t)$ or spin-up, $P_\uparrow(t)$ at time t follows from rate equations: (1) $\frac{dP_\uparrow}{dt} = -\Gamma^\uparrow_{out} P_\uparrow + 1/T_1 P_\downarrow$ and (2) $\frac{dP_\downarrow}{dt} = -(\Gamma^\downarrow_{out} + \frac{1}{T_1}) P_\downarrow$ with the initial conditions given by $P_\uparrow(t = 0\text{ns}) = 0$ and $P_\downarrow(t = 0\text{ns}) = 1$. From this we find $P_\uparrow(t) = \frac{1}{1 + T_1(\Gamma^\downarrow_{out} - \Gamma^\uparrow_{out})} e^{-\Gamma^\uparrow_{out} t} - e^{-(\frac{1}{T_1} + \Gamma^\downarrow_{out})t}$ and $P_\downarrow(t) = e^{-\left(\frac{1}{T_1} + \Gamma^\downarrow_{out}\right)t}$.

The resulting pulse in the QPC current with duration τ will be detected with probability $\mathcal{F}(\tau)$, which depends on the measurement bandwidth (see below). Therefore, the probability that a pulse which is caused by a spin-down electron that tunnels out is

detected is

$$\Xi^{1st} = \int_0^{T_R} \Gamma_{out}^{\downarrow} P_{\downarrow}(t) \int_0^{T_R - t} \Gamma_{in}^{\uparrow} e^{-\Gamma_{in}^{\uparrow}\tau} \mathcal{F}(\tau) d\tau dt \ . \tag{S3}$$

The probability that a spin-down electron relaxes during the read-out stage before it could tunnel out but that nevertheless a step is detected due to the spin-up electron tunneling out is given by

$$\Lambda^{1st} = \int_0^{T_R} \Gamma_{out}^{\uparrow} P_{\uparrow}(t) \int_0^{T_R - t} \Gamma_{in}^{\uparrow} e^{-\Gamma_{in}^{\uparrow}\tau} \mathcal{F}(\tau) d\tau dt \tag{S4}$$

where $\Gamma_{out}^{\uparrow} P_{\uparrow}(t)$ is the probability density function that the initial spin-down electron has relaxed to spin-up before tunneling out.

Note that for the first read-out stage we exclude all cycles in which an electron tunnels out, but the dot is not refilled at the end of the stage (see part B.3 of this supporting material and the main text). However, for the second read-out stage this postselection is not necessary and hence not applied. Therefore, Ξ for the second read-out stage is given by

$$\Xi^{2nd} = \int_0^{T_R} \Gamma_{out}^{\downarrow} P_{\downarrow} \int_0^{\infty} \Gamma_{in}^{\uparrow} e^{-\Gamma_{in}^{\uparrow}\tau} \mathcal{F}(\tau) d\tau dt \tag{S5}$$

where the upper limit of the inner integral is extended to ∞. Similarly, Λ for the second read-out stage is given by

$$\Lambda^{2nd} = \int_0^{T_R} \Gamma_{out}^{\uparrow} P_{\uparrow} \int_0^{\infty} \Gamma_{in}^{\uparrow} e^{-\Gamma_{in}^{\uparrow}\tau} \mathcal{F}(\tau) d\tau dt \ . \tag{S6}$$

The spin-down fidelity of the second read-out stage is additionally affected by relaxation during the first read-out stage, which has a duration T_R^{1st}. This relaxation occurs with probability $\eta = \int_0^{T_R^{1st}} \frac{1}{T_1} e^{-\frac{t}{T_1}} dt$. Therefore, the spin down fidelity for the quantum dot which is read out second is

$$\mathcal{F}_{\downarrow}^{2nd} = (\Xi^{2nd} + \Lambda^{2nd})(1 - \eta) + \eta \alpha^{2nd} \ . \tag{S7}$$

The last term accounts for the case that the spin down electron of the second dot relaxes during the first read-out stage but in the end it is still detected as a spin down.

To maximize the read-out fidelities, the quantum dot with the longer relaxation time (here the left dot) is read out in the second stage (minimizing η), the barriers for the left dot were set slower than those of the right dot and the second read-out stage is longer than the first (typically $T_R^{1st} = 1 - 2$ ms and $T_R^{2nd} = 1.5 - 2$ ms). The above expressions for the respective fidelities served as guides for tuning each tunnel barrier and for choosing the duration of the two read-out stages in such a way that the average measurement fidelity was optimized.

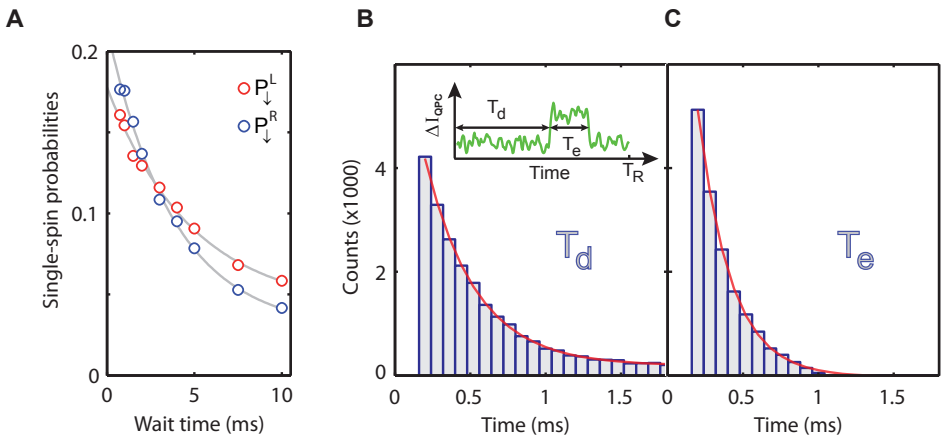

Figure S3: (A) Single dot relaxation as a function of wait time. Grey lines are fits to $\rho \cdot e^{-t/T_1} + \alpha$. (B) Histogram showing the distribution of the time T_d it takes a spin-down electron to tunnel out. The red line is an exponential fit from which we can find the decay rate given by $\Gamma_{out}^{\downarrow} + \frac{1}{T_1}$. Inset: real time trace of one of the read out stages indicating the detection time (T_d) and the event time (T_e). (C) Histogram showing the distribution of the time T_e it takes a spin-up electron to tunnel back into the empty dot. The red line is an exponential fit from which we can extract the decay rate given by $\Gamma_{in}^{\uparrow}$.

C.2 Determination of the tunnel rates

For calculating the spin-down read-out fidelities, various tunneling rates need to be known. We can obtain $\Gamma_{out}^{\downarrow}$ and $\Gamma_{in}^{\uparrow}$ from the measurements using histograms of the

time it takes a spin-down electron to tunnel out (T_d) and of the time it takes a spin-up electron to tunnel back into the quantum dot (T_e), see Figure S3B and S3C. We estimate $\Gamma^{\uparrow}_{out}$ from the measured value of α, which characterizes the spin up fidelities and can be expressed as

$$\alpha = \int_0^{T_R} \Gamma^{\uparrow}_{out} e^{-\Gamma^{\uparrow}_{out} t} \int_0^{T_M} \Gamma^{\uparrow}_{in} e^{-\Gamma^{\uparrow}_{in} \tau} \mathcal{F}(\tau) d\tau dt + \epsilon \, . \tag{S8}$$

Here ϵ is the signal processing error ($\epsilon \lesssim 0.5\%$, to be discussed in the section on measurement bandwidth characterization). T_M is equal to $T_R - t$ for the first read-out stage and is equal to infinity for the second read-out stage.

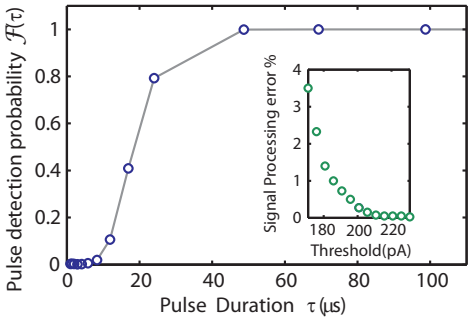

Figure S4: The probability of detecting a pulse with duration τ (grey line is a guide to the eye). Inset: signal processing error, ϵ, for different values of the threshold (see section B.2 on how the threshold is chosen).

C.3 Characterization of the measurement bandwidth

The signature of a spin-down electron tunneling out of the dot followed by a spin-up electron tunneling back into the dot is a pulse in the QPC current. Due to the finite measurement bandwidth, we can only detect pulses of sufficient duration and we therefore miss a fraction of the actual tunnel events. We characterize the measurement bandwidth by simulating such electron tunneling events by applying a rectangular pulse to the plunger gate with duration τ and amplitude A. The double dot is tuned deep into the (1,1) charge state such that the applied pulse cannot result in a charge transition of

any of the quantum dots. Due to the capacitive coupling of the plunger gate to the QPC, a rectangular pulse will be created in the QPC current. The amplitude A is chosen such that the height of the pulse in the QPC current equals the signal from electron tunneling events. The pulse duration is varied from 0 μs to 100 μs. Fig. S4 shows the probability of detecting an event of duration τ, $\mathcal{F}(\tau)$, as a function of the pulse duration. Using the formulas derived in C.1 we calculate the fidelities numerically by using the measured probabilities $\mathcal{F}(\tau)$ (we interpolate linearly between the data points).

The fraction of the detected events at $\tau = 0$ ns gives the signal processing error, ϵ (Fig. S4 inset), which corresponds to the fraction of traces in which an event is detected due to noise in the QPC current during the read-out stage. For all thresholds used in our data analysis, the signal processing error was less than 0.5%.

D Error analysis of truth table in Fig. 4E

D.1 Construction of the truth table

In this section we describe how we obtain the truth tables shown in Fig. 4E and 4F from the measured exchange oscillations shown in Fig. 4A-D. For each of the four measurements, referred to by the labels A-D in the following, the two spins are initialized in a different mixture. We therefore define four input vectors $\vec{P}^i_{in}$ (here $i = A, B, C, D$) and four output vectors $\vec{P}^i_{out,\pi}$ and $\vec{P}^i_{out,2\pi}$ corresponding to a π and 2π rotation of the exchange gate, respectively. They each contain four elements corresponding to the two-spin probabilities $P_{\uparrow\uparrow}$, $P_{\uparrow\downarrow}$, $P_{\downarrow\uparrow}$ and $P_{\downarrow\downarrow}$. We determine $\vec{P}^i_{in}$ by averaging the first three

points in each measurement, whereas $\vec{P}^i_{out,\pi}$ and $\vec{P}^i_{out,2\pi}$ are obtained from the values of the fit at the first maximum and minimum, respectively.

The first step to construct the truth table is to calculate the "true" input and output vectors, $\vec{\Pi}^i_{in}$, $\vec{\Pi}^i_{out,\pi}$ and $\vec{\Pi}^i_{out,2\pi}$, by compensating for the read-out fidelities. The four read-out fidelities $\mathcal{F}^L_\uparrow$, $\mathcal{F}^L_\downarrow$, $\mathcal{F}^R_\uparrow$ and $\mathcal{F}^R_\downarrow$ are estimated as described in section C of this supporting material. We find $\vec{\Pi}^i_{in}$ by solving the linear equations $\vec{P}^i_{in} = \mathbf{F} \cdot \vec{\Pi}^i_{in}$ where we introduced the matrix

$$\mathbf{F} = \begin{pmatrix} \mathcal{F}^L_\uparrow \cdot \mathcal{F}^R_\uparrow & \mathcal{F}^L_\uparrow \cdot (1-\mathcal{F}^R_\downarrow) & (1-\mathcal{F}^L_\downarrow) \cdot \mathcal{F}^R_\uparrow & (1-\mathcal{F}^L_\downarrow) \cdot (1-\mathcal{F}^R_\downarrow) \\ \mathcal{F}^L_\uparrow \cdot (1-\mathcal{F}^R_\uparrow) & \mathcal{F}^L_\uparrow \cdot \mathcal{F}^R_\downarrow & (1-\mathcal{F}^L_\downarrow) \cdot (1-\mathcal{F}^R_\uparrow) & (1-\mathcal{F}^L_\downarrow) \cdot \mathcal{F}^R_\downarrow \\ (1-\mathcal{F}^L_\uparrow) \cdot \mathcal{F}^R_\uparrow & (1-\mathcal{F}^L_\uparrow) \cdot (1-\mathcal{F}^R_\downarrow) & \mathcal{F}^L_\downarrow \cdot \mathcal{F}^R_\uparrow & \mathcal{F}^L_\downarrow \cdot (1-\mathcal{F}^R_\downarrow) \\ (1-\mathcal{F}^L_\uparrow) \cdot (1-\mathcal{F}^R_\uparrow) & (1-\mathcal{F}^L_\uparrow) \cdot \mathcal{F}^R_\downarrow & \mathcal{F}^L_\downarrow \cdot (1-\mathcal{F}^R_\uparrow) & \mathcal{F}^L_\downarrow \cdot \mathcal{F}^R_\downarrow \end{pmatrix} \tag{S9}$$

The linear equations are solved by numerically minimizing the squared length of the vector $\vec{P}^i_{in} - \mathbf{F} \cdot \vec{\Pi}^i_{in}$ and restricting the solutions $\vec{\Pi}^i_{in}$ to physical solutions (all elements have to be positive and the sum of the elements have to be one, since the vector consists of four two-spin probabilities). In the same way as $\vec{\Pi}^i_{in}$ we also find $\vec{\Pi}^i_{out,\pi}$ and $\vec{\Pi}^i_{out,2\pi}$. From the "true" input and output vectors we can determine the two different truth tables presented in Fig. 4E and F by solving another set of linear equations. To find the truth table corresponding to a π rotation of the exchange gate, $\mathbf{M}_\pi$, we solve the set of equations given by $\{\vec{\Pi}^i_{out,\pi} = \mathbf{M}_\pi \cdot \vec{\Pi}^i_{in})\}_{i=A,B,C,D}$. Again we solve this set of equations numerically by minimizing the sum of the squared lengths of the four vectors $\{\vec{\Pi}^i_{out,\pi} - \mathbf{M}_\pi \cdot \vec{\Pi}^i_{in})\}_{i=A,B,C,D}$, while restricting the elements of $\mathbf{M}_\pi$ to be positive and the sum of each column to be one. Using the data from Fig. 4A-D and the fidelities given in the main text we find the experimental truth table which is visualized in Fig.

4E:

$$\mathbf{M}_{\pi}^{0} = \begin{pmatrix} 1.00 & 0.03 & 0.00 & 0.00 \\ 0.00 & 0.62 & 0.39 & 0.28 \\ 0.00 & 0.33 & 0.60 & 0.00 \\ 0.00 & 0.02 & 0.01 & 0.72 \end{pmatrix} \tag{S10}$$

In the same way we determine the truth table corresponding to a 2π rotation of the exchange gate which is visualized in Fig. 4F:

$$\mathbf{M}_{2\pi}^{0} = \begin{pmatrix} 0.99 & 0.02 & 0.00 & 0.24 \\ 0.01 & 0.92 & 0.02 & 0.00 \\ 0.00 & 0.04 & 0.98 & 0.00 \\ 0.00 & 0.02 & 0.00 & 0.76 \end{pmatrix} \tag{S11}$$

D.2 Error analysis

Errors in the estimated fidelities and input and output vectors will result in errors in the truth table. In this section we analyze how sensitive the elements of the truth table $\mathbf{M}_{\pi}^{0}$ are to variations of the fidelities and the input and output vectors. In Fig. S5 we show the elements of truth tables $\mathbf{M}_{\pi}^{\delta}$ which are constructed in the same way as $\mathbf{M}_{\pi}^{0}$ while we change either an element of the input or output vector or one of the fidelities. Each element of the input and output vectors is varied by $\pm 1\%$ which is in the range of the statistical errors we find for the measured probabilities. The four fidelities are varied by plus or minus one standard deviation (values given in the main text). From the difference $\mathbf{M}_{\pi}^{\delta} - \mathbf{M}_{\pi}^{0}$ we can determine an error $\mathbf{E}_{\pi}(i,j)$ for each element $\mathbf{M}_{\pi}^{0}(i,j)$ (where (i,j) are indices labeling the element) in the following way: $\mathbf{E}_{\pi}(i,j) = \sqrt{\sum_{\delta}(\mathbf{M}_{\pi}^{\delta}(i,j) - \mathbf{M}_{\pi}^{0}(i,j))^2}$ where δ runs over all variations shown in Fig. S5. This results in:

$$\mathbf{E}_{\pi} = \begin{pmatrix} 0.03 & 0.14 & 0.01 & 0.19 \\ 0.00 & 0.07 & 0.07 & 0.27 \\ 0.02 & 0.13 & 0.10 & 0.00 \\ 0.00 & 0.05 & 0.04 & 0.25 \end{pmatrix} \tag{S12}$$

Note that here we assume that the errors are uncorrelated, which is not true for the variations on the input and output vectors. However we still show $\mathbf{E}_{\pi}$ for illustration

purposes. From $\mathbf{E}_\pi$ and Fig. S5 it is visible, that especially the last column of the truth table is very sensitive to variations in the input and output vectors. This column describes what the output of the gate is when acting on the two spins prepared in $\downarrow\downarrow$. The measurement which gives information on this last column of the truth table is the measurement shown in Fig. 4D. In Fig. 4D, the two spins are initialized in a mixture of all four spin states. However the occupation of $\downarrow\downarrow$ is low (see Fig. 4D) in this measurement, because the probability to inject spin-down in each dot is less than 50%. This limits the accuracy with which we can determine the last column of the truth table $\mathbf{M}_\pi^0$.

A similar analysis can be done for $\mathbf{M}_{2\pi}^0$.

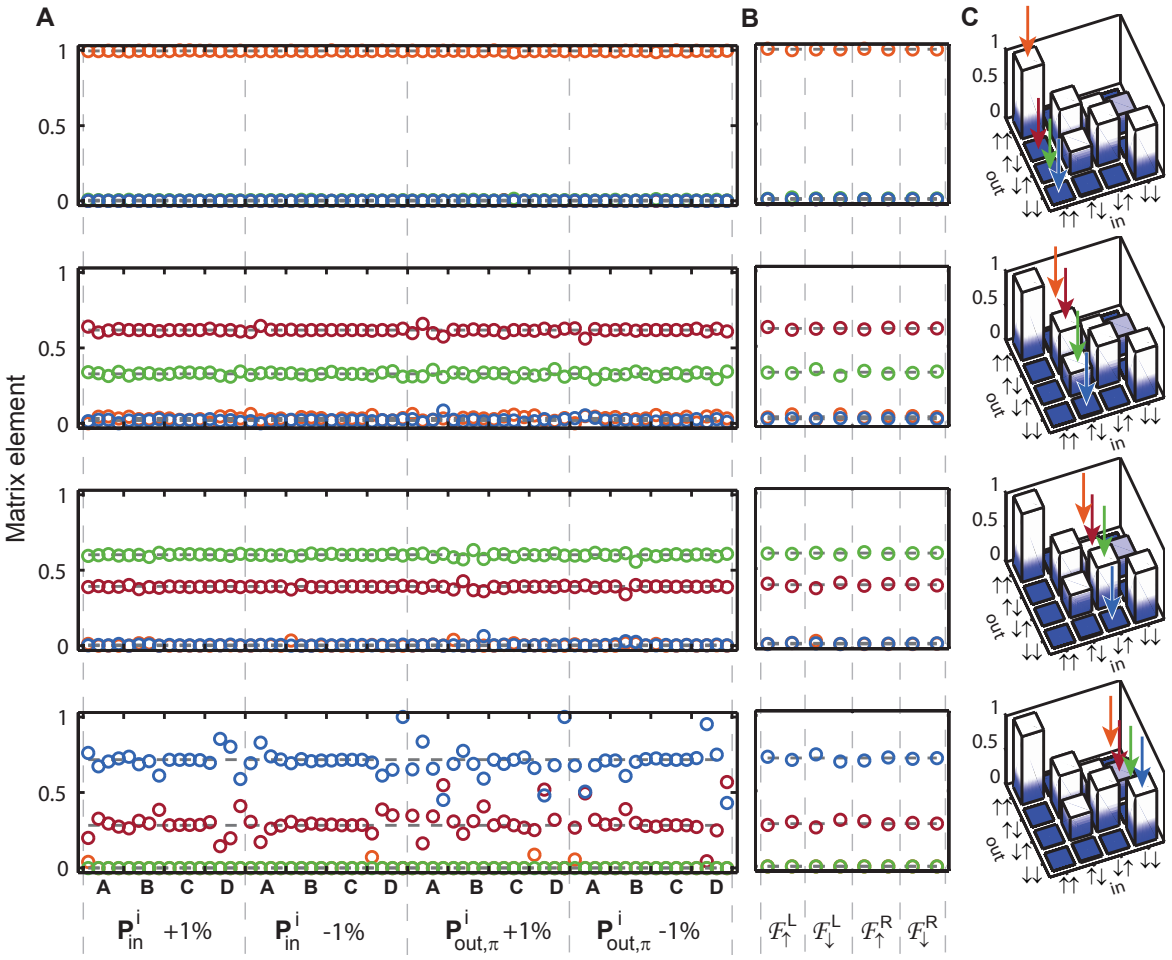

Figure S5: Shown are the elements of the truth table when varying (A) the input and output vectors and (B) the read-out fidelities. The four elements of each column of the truth table are shown in a separate plot as indicated in (C). (A) Each graph consists of four blocks in which $\vec{P}^i_{in}$ or $\vec{P}^i_{out,\pi}, i = A, B, C, D$ are varied element by element by $\pm 1\%$ as indicated below the graph. When varying one element by e.g. $+1\%$ we subtract $1/3\%$ from all other elements of the corresponding vector to ensure that all probabilities add up to one. If an element either becomes larger than one or smaller than 0 by this procedure, we set it to one and zero respectively and renormalize the vector. (B) Each graph consists of four parts corresponding to varying one of the read-out fidelities as indicated below the graph. We vary the fidelities by one standard deviation (added, respectively substracted for the two datapoints in each category).

E References and Notes

1. M. Nielsen, I. Chuang, *Quantum computation and information* (Cambridge University Press, Cambridge, UK, 2000).
2. P. W. Shor, *Proceedings of 35th Annual Symposium on Foundations of Computer Science, IEEE Press* pp. 124--134 (1994).
3. R. Hanson, L. P. Kouwenhoven, J. R. Petta, S. Tarucha, L. M. K. Vandersypen, *Rev. Mod. Phys.* **79**, 1217 (2007).
4. R. Hanson, D. Awschalom, *Nature* **453**, 1043 (2008).
5. D. Rugar, R. Budakian, H. Mamin, B. Chui, *Nature* **430**, 329 (2004).
6. A. Heinrich, J. Gupta, C. Lutz, D. Eigler, *Science* **306**, 466 (2004).
7. F. Meier, L. Zhou, J. Wiebe, R. Wiesendanger, *Science* **320**, 82 (2008).
8. F. Jelezko, T. Gaebel, I. Popa, A. Gruber, J. Wrachtrup, *Phys. Rev. Lett.* **92**, 076401 (2004).
9. J. Berezovsky *et al.*, *Science* **314**, 1916 (2006).
10. M. Atatüre, J. Dreiser, A. Badolato, A. Imamoglu, *Nature Phys.* **3**, 101 (2007).
11. R. Hanson *et al.*, *Phys. Rev. Lett.* **91**, 196802 (2003).
12. R. M. Potok *et al.*, *Phys. Rev. Lett.* **91**, 16802 (2003).
13. H. Sellier *et al.*, *Phys. Rev. Lett.* **97**, 206805 (2006).
14. J. M. Elzerman *et al.*, *Nature* **430**, 431 (2004).
15. C. Simmons *et al.*, *Phys. Rev. Lett.* **106**, 156804 (2011).
16. A. Morello *et al.*, *Nature* **467**, 687 (2010).
17. P. Neumann *et al.*, *Science* **329**, 542 (2010).
18. A. Vamivakas *et al.*, *Nature* **467**, 297 (2010).
19. R. Hanson *et al.*, *Phys. Rev. Lett.* **94**, 196802 (2005).
20. C. Barthel, D. J. Reilly, C. M. Marcus, M. P. Hanson, A. C. Gossard, *Phys. Rev. Lett.* **103**, 160503 (2009).
21. T. H. Oosterkamp *et al.*, *Nature* **395**, 873 (1998).
22. Information on materials and methods is available on *Science* Online.

23. We can also bring both dots into the read-out configuration simultaneously, making read-out faster but signal analysis more challenging, as tunneling from the left versus right dot has to be distinguished.
24. S. Amasha *et al.*, *Phys. Rev. B* **78** (2008).
25. J. R. Petta *et al.*, *Science* **309**, 2180 (2005).
26. D. Taubert *et al.*, *Phys. Rev. Lett.* **100**, 176805 (2008).
27. J. Taylor *et al.*, *Nature Phys.* **1**, 177 (2005).
28. D. Loss, D. P. DiVincenzo, *Phys. Rev. A* **57**, 120 (1998).
29. S. Foletti, H. Bluhm, D. Mahalu, V. Umansky, A. Yacoby, *Nature Phys.* **5**, 903 (2009).
30. A. Khaetskii, Y. Nazarov, *Phys. Rev. B* **64**, 125316 (2001).
31. D. Reilly, C. Marcus, M. Hanson, A. Gossard, *Appl. Phys. Lett.* **91**, 162101 (2007).
32. C. Barthel *et al.*, *Phys. Rev. B* **81**, 161308 (2010).
33. H.-A. Engel *et al.*, *Phys. Rev. Lett.* **93**, 106804 (2004).
34. L. M. K. Vandersypen *et al.*, *Appl. Phys. Lett.* **85**, 4394 (2004).
35. H. Ho, W. P. McCormick, *J. Appl. Prob.* **36**, 1031 (1999).